Supporting Information for

Long-term InSAR and streamflow recession analysis reveal accelerated permafrost degradation in the mining area of Qilian Mountain

Tian Chang[1,2,3], Yonghong Yi[1,2], Masato Furuya[4,5], Huiru Jiang[1,2], Tao Che[6], Youhua Ran[6], Lin Liu[7], Rongxing Li[1,2]

[1]Center for Spatial Information Science and Sustainable Development Applications, Tongji University, Shanghai, 200092, China.

[2]College of Surveying and Geo-informatics, Tongji University, Shanghai, 200092, China

[3]Graduate School of Science, Hokkaido University, Sapporo, 060-0810, Japan

[4]Department of Earth and Planetary Sciences, Faculty of Science, Hokkaido University, Sapporo, 060-0810, Japan

[5]Arctic Research Center, Hokkaido University, Sapporo, 001-0021, Japan

[6]Heihe Remote Sensing Experimental Research Station, State Key Laboratory of Cryospheric Science and Frozen Soil Engineering, Northwest Institute of Eco-Environment and Resources, Chinese Academy of Sciences, Lanzhou, 730000, China

[7]Department of Earth and Environmental Sciences, Faculty of Science, The Chinese University of Hong Kong, Hong Kong, China

Correspondence to: Yonghong Yi (yonghong_yi@tongji.edu.cn)

Contents of this file

The supplementary material includes Table S1 and Figs. S1 to S13 that support the main manuscript.

Table S1: The information of interferograms obtained from ERS-2, Envisat, ALOS-1, and ALOS-2.
Figure S1: Multispectral unmanned aerial vehicle (UAV) survey of surface conditions around the mining area.
Figure S2: Sentinel-1 interferogram network and average spatial coherence.
Figure S3: Cumulative distribution function matching between Sentinel-1 and ALOS-2 deformation rates.
Figure S4: Comparison between actual observed thaw-season deformation and thaw-season deformation scaled using the thawing index.
Figure S5: Time series of streamflow recession time constant and model goodness-of-fit obtained using 1-year fitting, 3-year moving-window fitting, and 5-year moving-window fitting.
Figure S6: The coherence maps of the interferograms from ALOS-1.
Figure S7: The coherence maps of the interferograms from ALOS-2.
Figure S8: Time series of cumulative surface deformation from 2016 to 2023.
Figure S9: Comparison between Sentinel-1 InSAR deformation time series and GNSS-IR (GNSS Interferometric Reflectometry) measurements at the Yakou station during the snow-free period in 2018.
Figure S10: Deformation trend and thaw season deformation around the open-pit mine in the western part of the study area.
Figure S11: Comparison of ground surface characteristics at the P1 site near the Jiangcang open-pit mine on July 24, 1984 from Keyhole-9 data and on July 16, 2025 from UAV data.
Figure S12: Vertical deformation rate maps during different periods.
Figure S13: Vertical thaw-season deformation maps during different periods.

Table S1 The information of interferograms obtained from ERS-2, Envisat, ALOS-1, and ALOS-2.

Satellite	Image 1 (dd/mm/yyyy)	Image 2 (dd/mm/yyyy)	Perpendicular baseline (m)	Time span (days)
ERS-2	19970428	19970602	98	35
	19970811	19980727	-239	350
Envisat	20031018	20051022	-435	735
ALOS-1	20070712	20071012	702	92
	20070712	20080714	-1053	368
	20070827	20090901	-853	736
	20070827	20100904	1225	1104
	20100720	20101020	481	92
ALOS-2	20190324	20200322	307	364
	20190519	20190714	-25	56
	20190714	20200322	386	252
	20200322	20210321	46	364
	20210321	20220320	-273	364

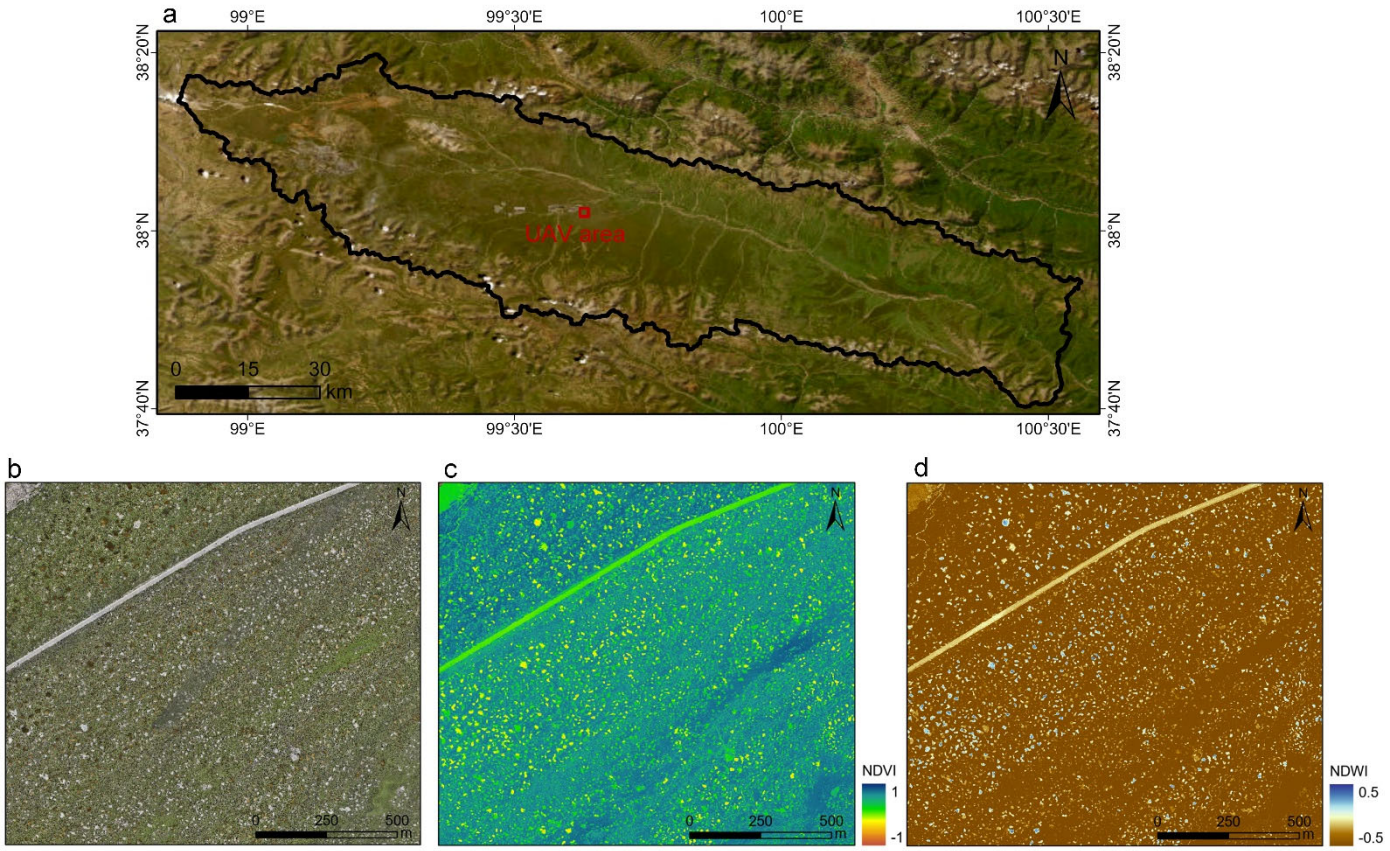

Figure S1 Multispectral unmanned aerial vehicle (UAV) survey of surface conditions around the mining area: (a) survey location, (b) orthophoto, (c) normalized difference vegetation index (NDVI), and (d) normalized difference water index (NDWI). The optical basemap in panel (a) is from Esri | Powered by Esri.

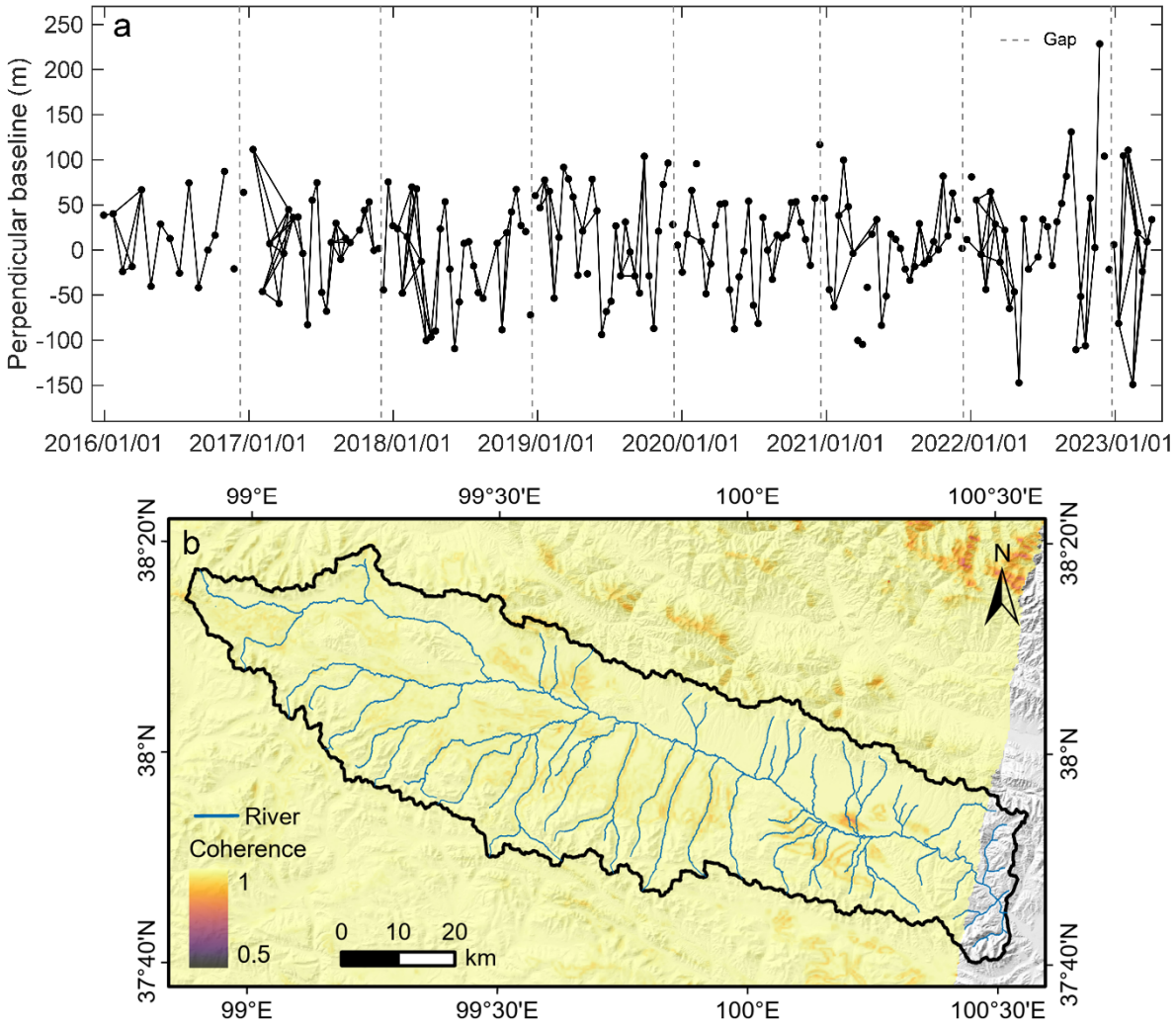

Figure S2 Sentinel-1 interferogram network (a) and average spatial coherence (b).

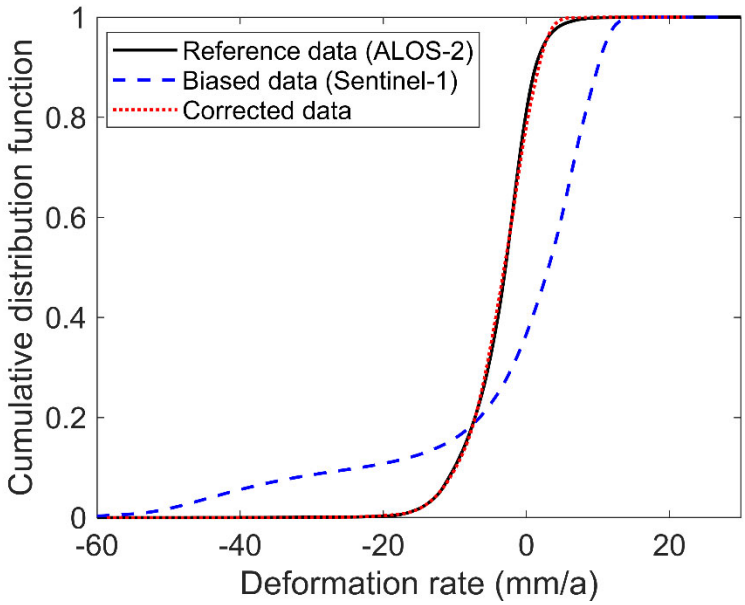

Figure S3 Cumulative distribution function (CDF) matching between Sentinel-1 and ALOS-2 deformation rates. The initial Sentinel-1 deformation rates were corrected to align with the reference ALOS-2 data.

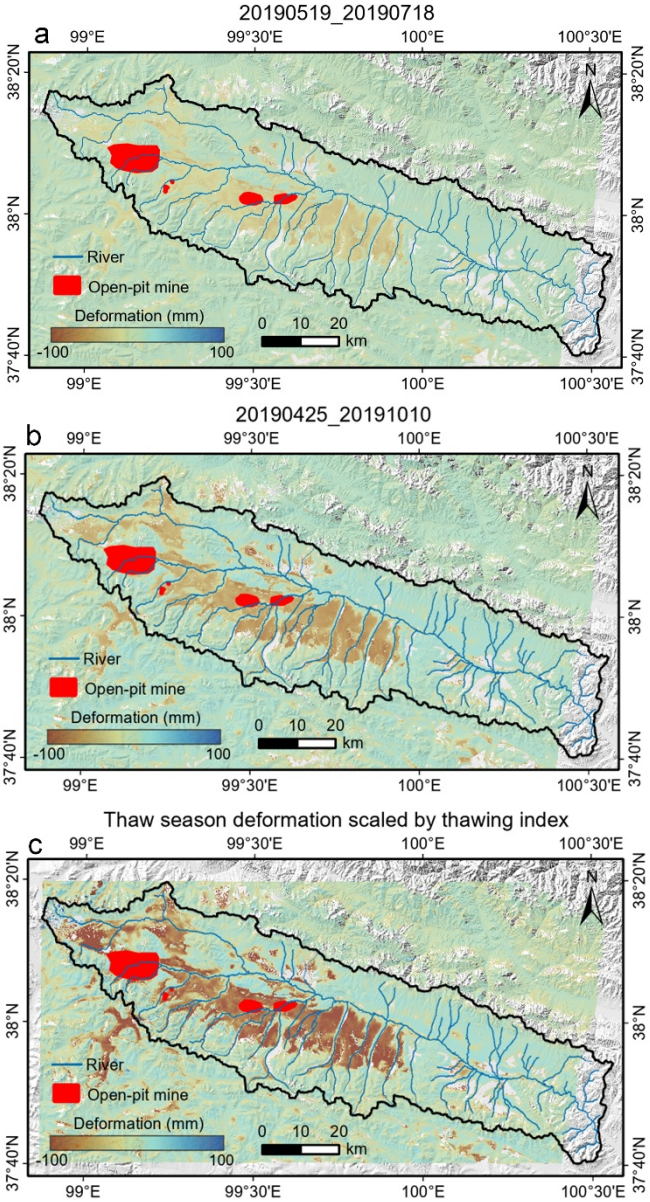

Figure S4 Comparison between actual observed thaw-season deformation and thaw-season deformation scaled using the thawing index. (a) Partial-season deformation from May–July 2019 derived from the Sentinel-1 interferogram network. (b) Actual observed thaw-season deformation in 2019 from Sentinel-1. (c) Thaw-season deformation scaled using the thawing index.

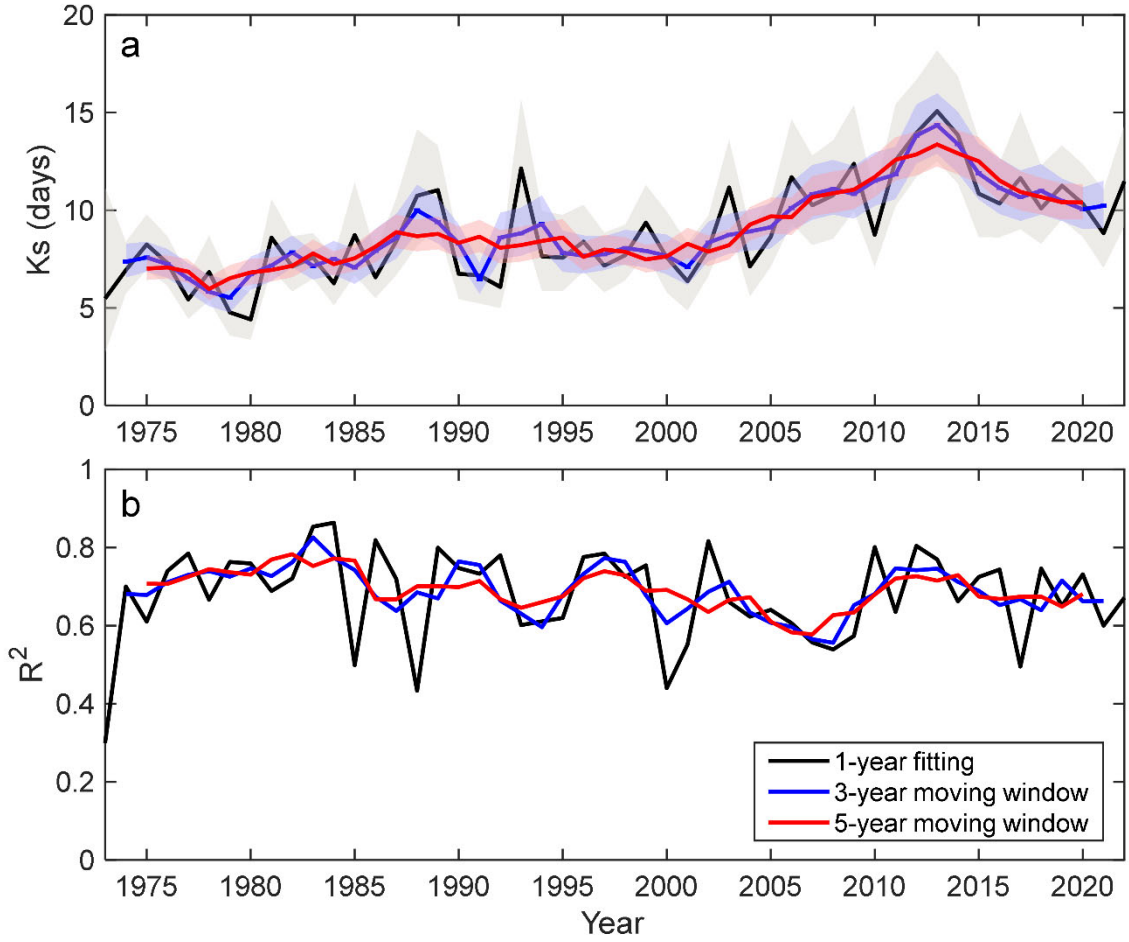

Figure S5 Time series of streamflow recession time constant (Ks) and model goodness-of-fit (R^2). (a) Ks time series derived from 1-year fitting (black line), 3-year moving-window fitting (blue line), and 5-year moving-window fitting (red line), with shaded areas representing the 95% confidence intervals. (b) Goodness-of-fit (R^2) of Ks estimates obtained using 1-year fitting (black line), 3-year moving-window fitting (blue line), and 5-year moving-window fitting (red line).

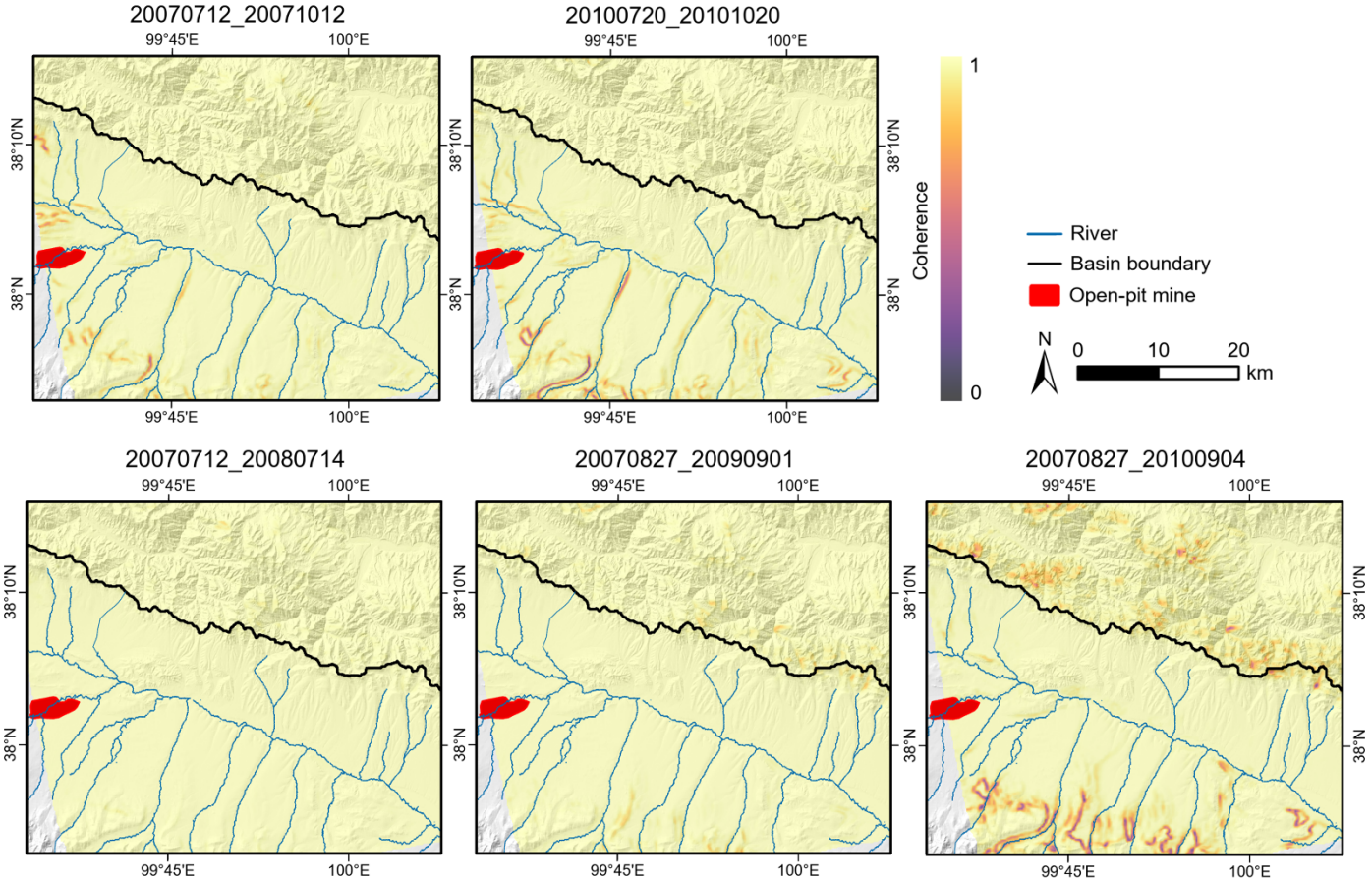

Figure S6 The coherence maps of the interferograms from ALOS-1.

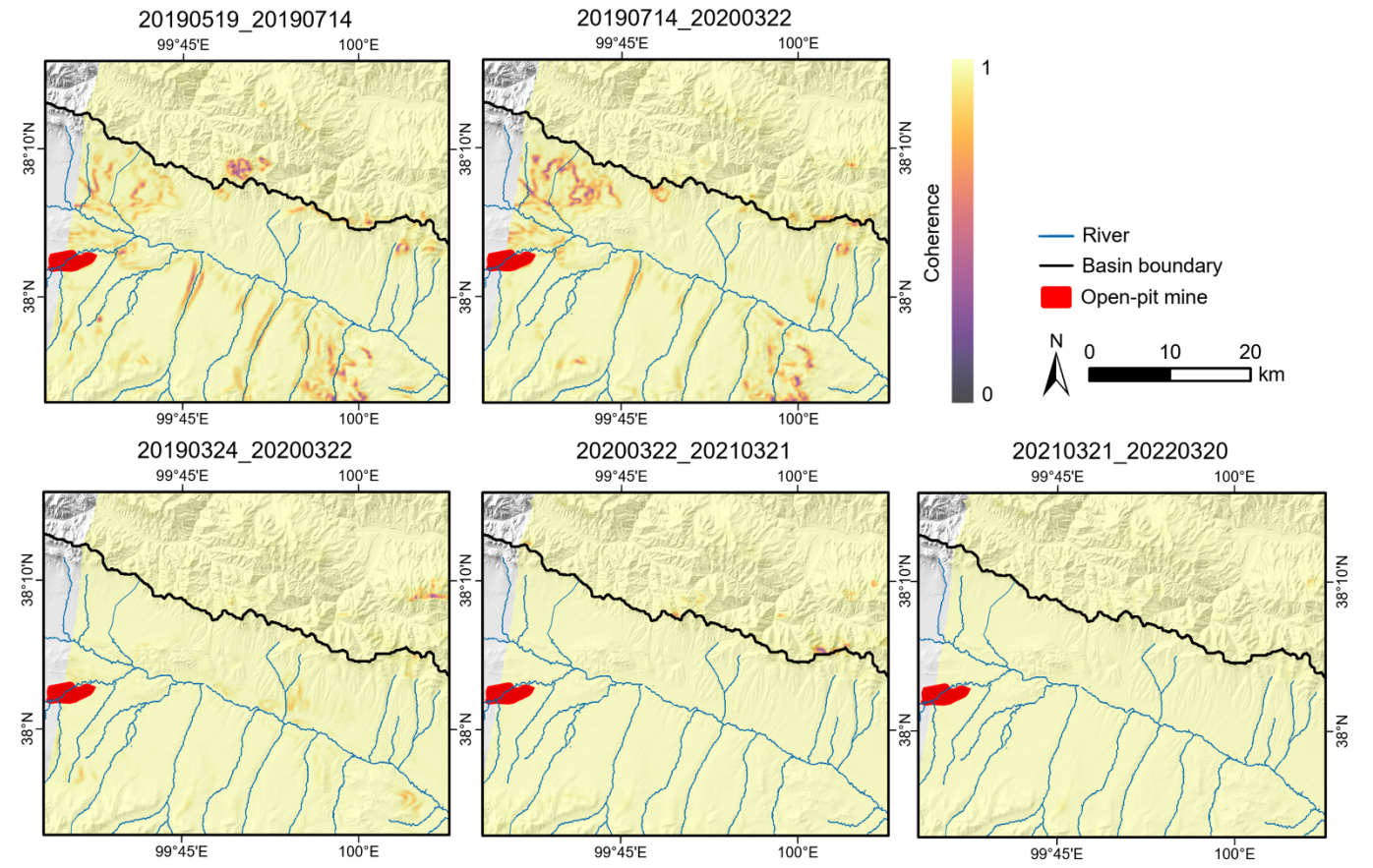

Figure S7 The coherence maps of the interferograms from ALOS-2.

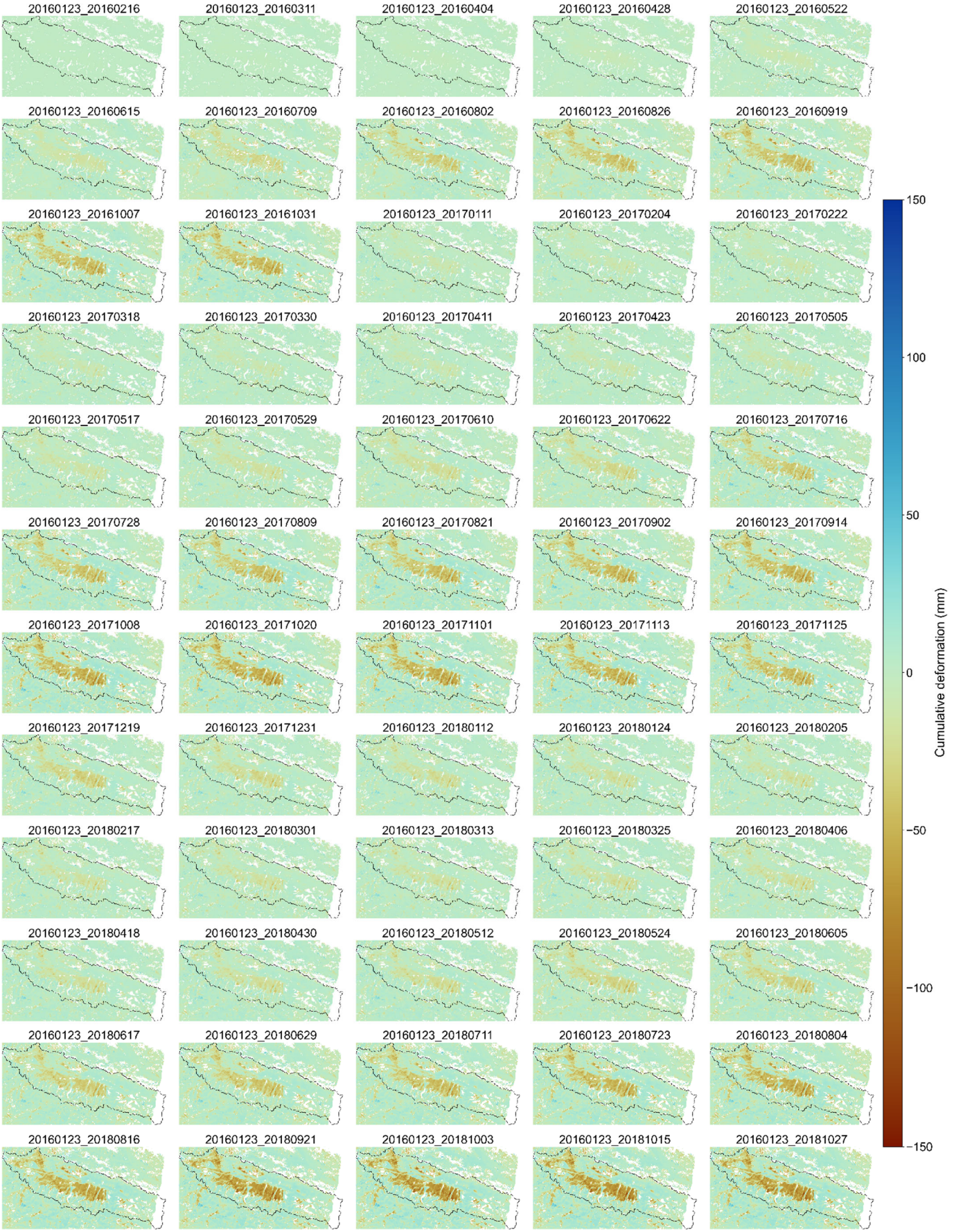
20160123_20160216
20160123_20160311
20160123_20160404
20160123_20160428
20160123_20160522
20160123_20160615
20160123_20160709
20160123_20160802
20160123_20160826
20160123_20160919
20160123_20161007
20160123_20161031
20160123_20170111
20160123_20170204
20160123_20170222
20160123_20170318
20160123_20170330
20160123_20170411
20160123_20170423
20160123_20170505
20160123_20170517
20160123_20170529
20160123_20170610
20160123_20170622
20160123_20170716
20160123_20170728
20160123_20170809
20160123_20170821
20160123_20170902
20160123_20170914
20160123_20171008
20160123_20171020
20160123_20171101
20160123_20171113
20160123_20171125
20160123_20171219
20160123_20171231
20160123_20180112
20160123_20180124
20160123_20180205
20160123_20180217
20160123_20180301
20160123_20180313
20160123_20180325
20160123_20180406
20160123_20180418
20160123_20180430
20160123_20180512
20160123_20180524
20160123_20180605
20160123_20180617
20160123_20180629
20160123_20180711
20160123_20180723
20160123_20180804
20160123_20180816
20160123_20180921
20160123_20181003
20160123_20181015
20160123_20181027
150
100
50
0
−50
−100
−150
Cumulative deformation (mm)

20160123_20181108
20160123_20181120
20160123_20181202
20160123_20181226
20160123_20190107
20160123_20190119
20160123_20190131
20160123_20190212
20160123_20190224
20160123_20190308
20160123_20190320
20160123_20190401
20160123_20190413
20160123_20190425
20160123_20190519
20160123_20190531
20160123_20190612
20160123_20190624
20160123_20190706
20160123_20190718
20160123_20190730
20160123_20190811
20160123_20190823
20160123_20190904
20160123_20190916
20160123_20190928
20160123_20191022
20160123_20191103
20160123_20191115
20160123_20191127
20160123_20191221
20160123_20200102
20160123_20200114
20160123_20200126
20160123_20200219
20160123_20200302
20160123_20200314
20160123_20200326
20160123_20200407
20160123_20200419
20160123_20200501
20160123_20200513
20160123_20200525
20160123_20200606
20160123_20200618
20160123_20200630
20160123_20200712
20160123_20200724
20160123_20200805
20160123_20200817
20160123_20200829
20160123_20200910
20160123_20200922
20160123_20201004
20160123_20201016
20160123_20201028
20160123_20201109
20160123_20201121
20160123_20201203
20160123_20201227
150
100
50
0
−50
−100
−150
Cumulative deformation (mm)

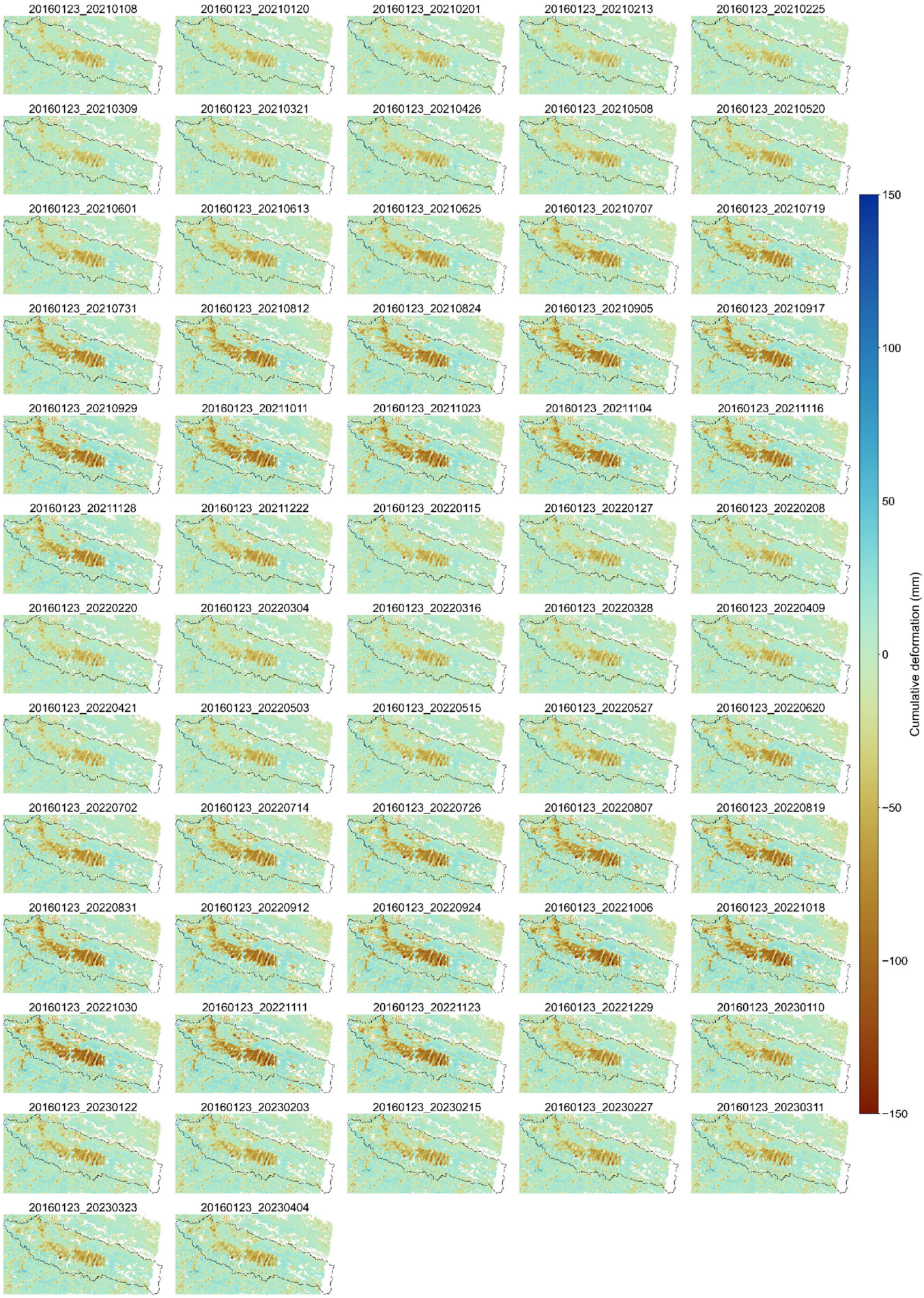

Figure S8 Time series of cumulative surface deformation from 2016 to 2023, referenced to the first acquisition date.

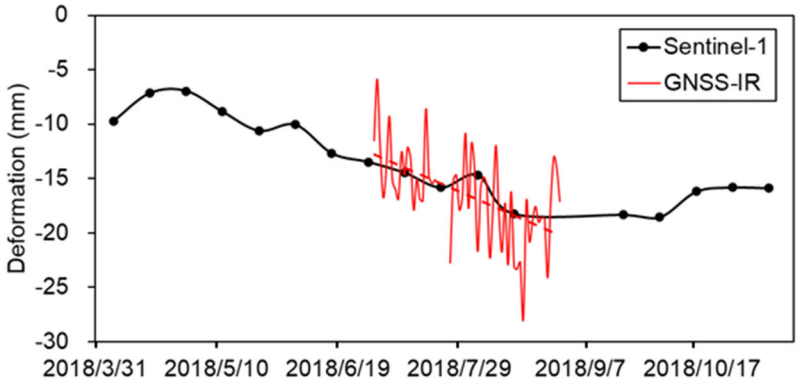

Figure S9 Comparison between Sentinel-1 InSAR deformation time series and GNSS-IR (GNSS Interferometric Reflectometry) measurements (Zhang et al., 2021) at the Yakou station during the snow-free period in 2018.

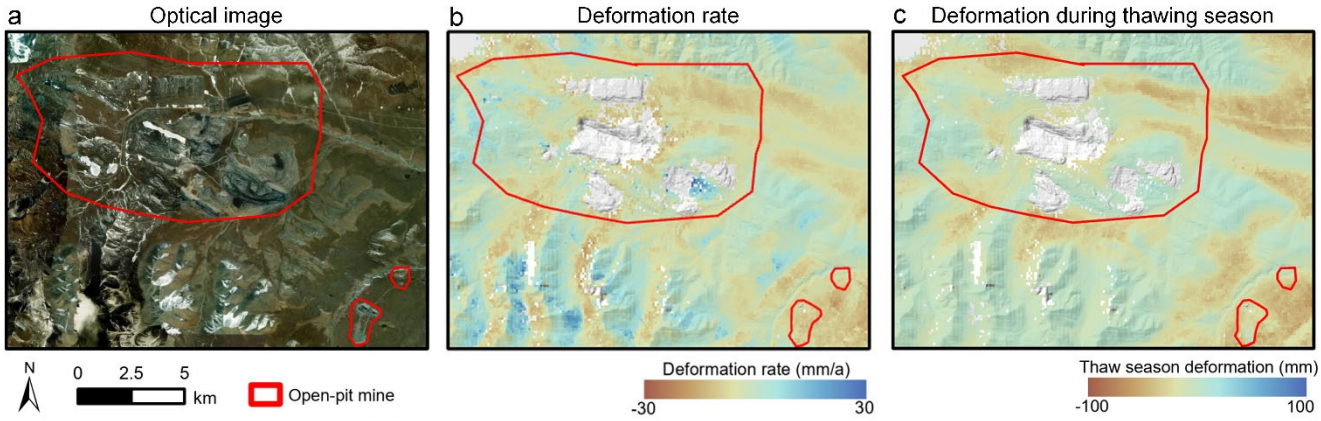

Figure S10 (a) Optical image of the open-pit mine in the western study area from Esri | Powered by Esri. (b) Deformation trend and (c) thaw-season deformation in its surroundings.

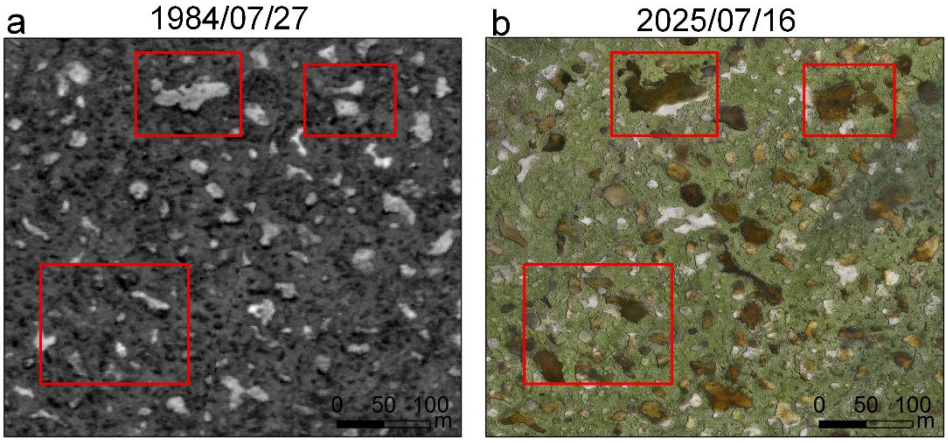

Figure S11 Comparison of ground surface characteristics at the P1 site near the Jiangcang open-pit mine on July 24, 1984 from Keyhole-9 data provided by the U.S. Geological Survey (a) and on July 16, 2025 from UAV data acquired by the authors (b).

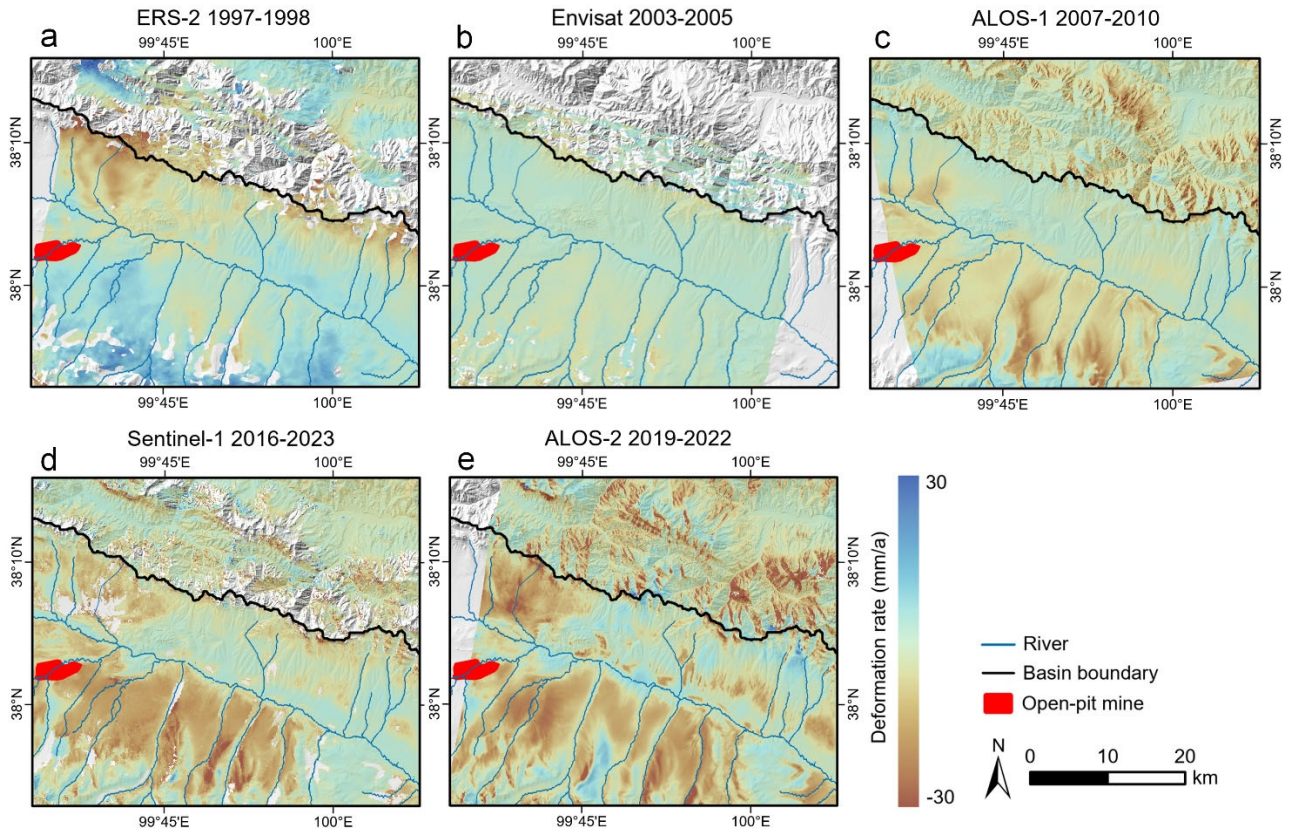

Figure S12 Vertical deformation rate maps during different periods derived from multi-source SAR data.

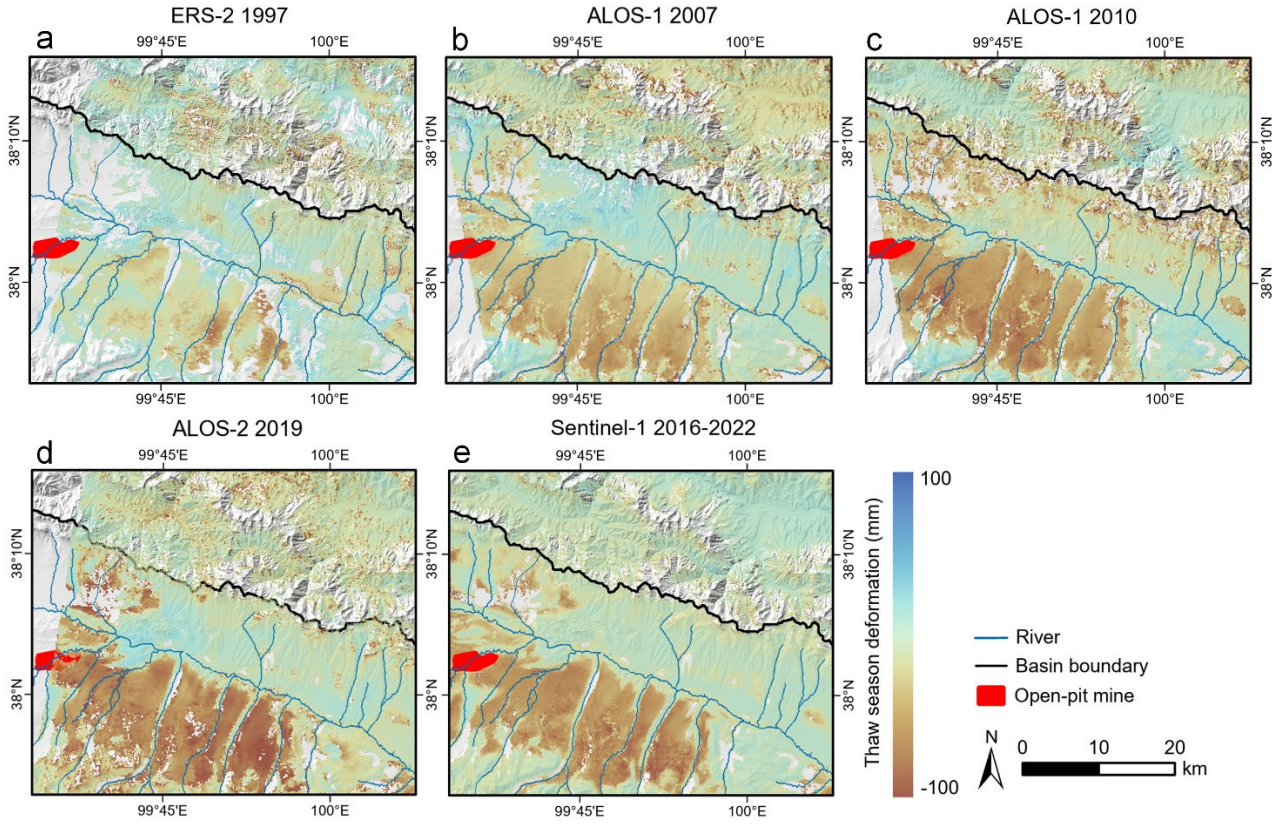

Figure S13 Vertical thaw-season deformation maps during different periods derived from multi-source SAR data.